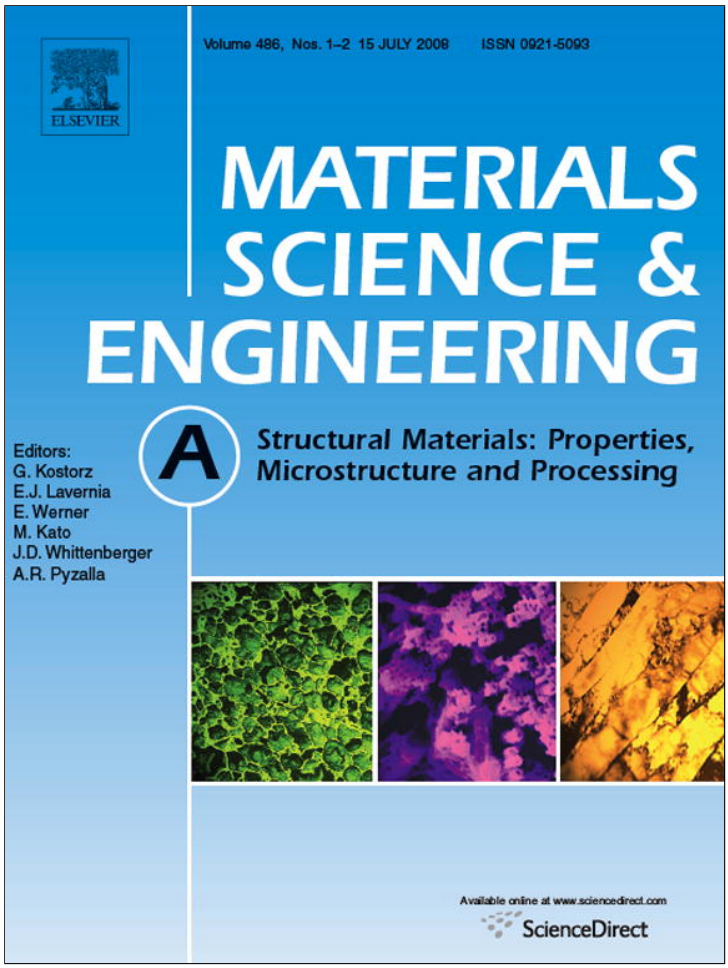

ELSEVIER

Materials Science and Engineering A 486 (2008) 389–403

MATERIALS SCIENCE & ENGINEERING A

www.elsevier.com/locate/msea

Effect of microstructure on the fatigue of hot-rolled and cold-drawn NiTi shape memory alloys

Ken Gall [a,*], Jeff Tyber [a], Geneva Wilkesanders [a], Scott W. Robertson [b], Robert O. Ritchie [b], Hans J. Maier [c]

[a] *Department of Materials Science and Engineering, Woodruff School of Mechanical Engineering, Georgia Institute of Technology, Atlanta, GA 30332, United States*

[b] *Department of Materials Science and Engineering, University of California, Berkeley, CA 94720, United States*

[c] *Lehrstuhl für Werkstoffkunde (Materials Science), University of Paderborn, 33095 Paderborn, Germany*

Received 8 May 2007; received in revised form 6 September 2007; accepted 6 November 2007

Abstract

We present results from a systematic study linking material microstructure to monotonic and fatigue properties of NiTi shape memory alloys. We consider Ni-rich materials that are either (1) hot rolled or (2) hot rolled and cold drawn. In addition to the two material processing routes, heat treatments are used to systematically alter material microstructure giving rise to a broad range of thermal, monotonic and cyclic properties. The strength and hardness of the austenite and martensite phases initially increase with mild heat treatment (300 °C), and subsequently decrease with increased aging temperature above 300 °C. This trend is consistent with transmission electron microscopy observed precipitation hardening in the hot-rolled material and precipitation hardening plus recovery and recrystallization in the cold-drawn materials. The low-cycle pseudoelastic fatigue properties of the NiTi materials generally improve with increasing material strength, although comparison across the two product forms demonstrates that higher measured flow strength does not assure superior resistance to pseudoelastic cyclic degradation. Fatigue crack growth rates in the hot-rolled material are relatively independent of heat treatment and demonstrate similar fatigue crack growth rates to other NiTi product forms; however, the cold-drawn material demonstrates fatigue threshold values some 5 times smaller than the hot-rolled material. The difference in the fatigue performance of hot-rolled and cold-drawn NiTi bars is attributed to significant residual stresses in the cold-drawn material, which amplify fatigue susceptibility despite superior measured monotonic properties.

Keywords: NiTi; Fatigue; Strength; Microstructure; Crack growth

1. Introduction

Nickel–titanium (NiTi) shape memory alloys possess the ability to recover strains on the order of 8% or more due to a highly reversible thermoelastic martensitic transformation. Depending on the testing temperature, NiTi demonstrates two different strain recovery responses: pseudoelasticity and shape memory. Pseudoelasticity (also termed superelasticity) refers to the spontaneous recovery of strains in initially austenitic NiTi upon removal of the applied stress, and is attributed to the reversible stress-induced austenite-to-martensite phase transformation. Shape memory describes the recovery of strains in initially austenitic or martensitic NiTi after unloading and subsequent heating above a critical temperature. A pseudoelastic response occurs when NiTi is deformed sufficiently above its austenite finish temperature, A_f, while shape memory is observed when NiTi is deformed below the martensite finish temperature (A_f). At temperatures sufficiently above A_f, and above the so-called martensite deformation temperature, M_d, NiTi deforms by elastic–plastic response (i.e., via dislocation motion) similar to conventional metallic materials.

The shape memory and particularly pseudoelastic properties of NiTi have led to a palette of innovative medical devices [1–6]. Orthodontic wires utilize the constant stress unloading response inherent to pseudoelasicity to provide a stable restraining force on teeth. Orthodontic drills and cardiovascular guidewires exploit local pseudoelastic strains to facilitate repeatable large-strain bending deformations without perma-

* Corresponding author. Fax: +1 404 894 9140.
E-mail address: ken.gall@mse.gatech.edu (K. Gall).

0921-5093/$ – see front matter © 2007 Elsevier B.V. All rights reserved.
doi:10.1016/j.msea.2007.11.033

nent kinking. Peripheral artery stents use pseudoelasticity to self-deploy inside an artery and provide improved crush resistance once implanted. Orthopedic staples use the shape memory effect to provide a clamping force at a fracture site and improve potential for bone union. Although the biocompatibility of NiTi has been extensively studied [7–26], the corresponding fatigue properties are not fully understood and have led to, for example, a surprising number of *in vivo* medical device fractures [27–29].

Basic macroscopic features of NiTi fatigue were established some 10–30 years ago [30–47]. During low-cycle pseudoelastic loading of NiTi, the critical transformation stress level decreases, the transformation stress–strain slope increases, the dissipated hysteresis energy decreases, and residual strains are accumulated. During low-cycle thermomechanical cycling, an applied stress causes the accumulation of transformation strain along the direction of the applied stress and also results in permanent plastic strains. The low-cycle fatigue behavior of NiTi is typically superior to traditional metals when the comparison is made based on strain amplitudes since the inelastic strains are produced by a reversible transformation rather than more dissipative dislocation activity [48]. Furthermore, NiTi is unique compared to most alloys because high-strength NiTi materials can also exhibit good low-cycle fatigue resistance due to the transformation; traditional metals are typically strengthened to a level to make them relatively more resistant to low or high-cycle fatigue. Early studies [30–45] have shown that the low-cycle fatigue response of NiTi depends on a number of variables such as strain range, heat treatment, temperature, mean stress, loading path, and control mode. On the other hand, NiTi has been shown to demonstrate only moderate resistance to high-cycle fatigue [45]. In particular, the fatigue crack growth rates in NiTi are typically faster compared to alternative biomedical implant materials [46,47,49–52].

More recent work has focused on developing a deeper understanding of fatigue in NiTi shape memory alloys. Due to the strong dependence of operant deformation mechanisms on the applied stress level, the terms ‘structural’ and ‘functional’ fatigue have been coined to help distinguish between high-cycle and low-cycle fatigue of NiTi [53,54]. Researchers have continued phenomenological-based rotary bend fatigue testing of NiTi due to the direct relevance to rotating medical devices [55–58]. Other related studies have examined the effect of mean strain [59] and deformation localization [60] on the low-cycle fatigue behavior of NiTi. A few studies have begun to more explicitly discuss the effect of microstructure on the fatigue resistance of NiTi, focusing on the effects of thermomechanical processing [61–65]. Although preliminary work has demonstrated the strong link between thermomechanical processing and fatigue of NiTi, the processing–structure–fatigue relationship is not fully developed for polycrystalline NiTi. For example, prior work [61–64] has shown that a cold-worked alloy with a higher monotonic strength shows better resistance to low-cycle pseudoelastic fatigue compared to a lower strength alloy. However, as will be shown in the present work, increased monotonic strength does not *always* correlate with higher resistance to low-cycle fatigue when comparing material processing routes.

Low-cycle fatigue studies on single crystal NiTi have revealed a strong relationship between microstructure and low-cycle fatigue response [66–69]. The crystallographic orientation (i.e., texture) of the specimens greatly influences the ability of NiTi to resist low-cycle fatigue. Optimal low-cycle fatigue response was observed for samples oriented most favorably (lowest required transformation stress) for the martensitic transformation and least favorably for dislocation motion. In addition, due to the asymmetric nature of the phase transformation, the direction of the applied stress (i.e., tension versus compression) influences the fatigue response of single crystal NiTi. Nickel rich NiTi materials contain Ni_4Ti_3 precipitates, and single crystal experiments have shown that precipitate size strongly influences low-cycle fatigue resistance by altering the relative resistance to the martensitic transformation and dislocation motion [66–69]. The aforementioned single crystal studies indicate that precipitate structure and crystallographic texture may have a significant influence on the fatigue behavior of polycrystalline NiTi.

There have been correspondingly fewer studies on the fatigue crack growth resistance of NiTi. Previous work on NiTi bar [46,47,49], sheet [50,70] and tubing [51,52] demonstrated remarkably low fatigue threshold stress intensity values ($\Delta K_{th} \sim 2$–$4\,\mathrm{MPa}\sqrt{\mathrm{m}}$) when compared with other biomaterials. However, none of these prior fatigue crack growth investigations revealed the role of mechanical processing and subsequent heat treatment on the fatigue crack growth in NiTi. In summary, although it is known that thermomechanical treatments alter fatigue properties, the link between the microstructures induced by these treatments and the resulting fatigue behavior and mechanisms is unclear, especially for alloys only strengthened by precipitation hardening (hot-rolled materials). The objective of the present paper is to provide an improved understanding of the effect of microstructure on the fatigue of NiTi shape memory alloys across different deformation processing routes.

2. Materials and methods

We employed a commercial polycrystalline NiTi with a nominal composition of Ti–50.9 at.%Ni (Ti–55.7 wt.%Ni). The material was first processed by hot rolling at temperatures between 845 °C and 955 °C. It was straightened and centerless ground to a final diameter of 31.8 mm. This material is referred to as “hot rolled”. A duplicate hot-rolled bar was subsequently cold drawn approximately 30%. It was then straightened and centerless ground to a diameter of 26.7 mm. This material is referred to as “cold drawn”. All test pieces were fabricated from the two bars by means of electro-discharge machining (EDM), and any residue from machining was removed by sanding prior to heat treatment. Hot-rolled and cold-drawn materials were studied with four different heat treatments: (a) as-received, (b) annealed in an air furnace 300 °C, (c) annealed in an air furnace 350 °C, and (d) annealed in an air furnace 550 °C. All heat treatments were performed for 1.5 h followed by a water quench. Hardness measurements were preformed with digital Rockwell hardness tester, using a C-scale diamond-tip indenter at room temperature.

Samples used for examination with transmission electron microscopy (TEM) were prepared by mechanical grinding and subsequent twin-jet electropolishing of 3 mm disks. Electropolishing was carried out using a 5% perchloric acid and 95% ethanol solution electrolyte at 35 V and −15 °C. The TEM samples were studied in an analytical transmission electron microscope operated at a nominal acceleration voltage of 200 kV. Whenever possible, the TEM images were recorded under two-beam conditions.

A differential scanning calorimeter (DSC) was used to determine the characteristics of thermally induced transformations. The DSC cycle was performed as follows: hold for 1 min at 20 °C, cool to −70 °C at 10 °C/min, hold for 2 min at −70 °C, heat to 150 °C at 10 °C/min, hold for 2 min at 150 °C, and cool to −70 °C at 10 °C/min. All DSC samples were cut using a cooled slow speed diamond wafer blade saw and mounted in high purity aluminum sample pans.

Monotonic and low-cycle fatigue samples were electro-discharge machined from hot-rolled and cold-drawn bars. The resulting oxide layer from the annealing and machining process was mechanically removed prior to thermal and mechanical testing. Flat dog bone tensile specimens, Fig. 1a, were designed from a scaled down version of ASTM E8 [71] standard design. The loading axis of the specimens was machined in the direction of the deformation processing. Monotonic tests were performed at room temperature (25 °C) and elevated temperature (125 °C or 150 °C) on the hot-rolled and cold-drawn samples, using a screw-driven mechanical load frame. Mechanical tests were conducted in strain and load control using a miniature extensometer with a 3 mm gauge length. Monotonic specimens were loaded until failure or 15% strain (at $10^{-3}\,s^{-1}$) and unloaded in load control (at 40 N/s) to 0.1 MPa if failure did not occur. Low-cycle fatigue experiments were conducted using a triangle wave function in strain control for loading and load control for unloading. Samples were loaded to 3.0% in strain control and unloaded to 0.0 MPa in load control. The wave function was repeated for 100 cycles at a frequency of approximately 0.17 Hz. Temperature was controlled during monotonic and low-cycle fatigue tests using a liquid nitrogen tube cooled, air heated thermal chamber.

Disk-shaped compact tension, C(T), specimens were electro-discharge machined from the bars such that the pre-notch was aligned in the radial direction (Fig. 1b), mechanically ground through 1200-grit paper to remove the machining and annealing oxides, and electropolished for a consistent finish. Fatigue crack propagation tests were carried out on an electro servo-hydraulic mechanical test system in general accordance with ASTM Standard E 647 [72], at a positive load ratio, $R = K_{min}/K_{max} = 0.1$, at 50 Hz (sine wave) frequency, in ambient air. A minimum of four test specimens were used to obtain each fatigue crack growth curve ($N \geq 4$). Crack lengths were continuously monitored via a back-face strain gauge on each sample. Most tests were conducted in load control to generate an increasing growth rate and stress intensity range with crack advance, with the exception being at near-threshold values where computer-controlled continuous force shedding was utilized at a K-gradient of $-0.20\,mm^{-1}$. Fatigue threshold ΔK_{th} values were operationally defined as the stress intensity range at which growth rates did not exceed 10^{-10} m/cycle [72].

3. Results and discussion

3.1. Microstructure

The hot-rolled and cold-drawn materials studied here have been previously characterized [65,73]. At the grain scale, both materials have a relatively strong ⟨1 1 1⟩ texture along their draw-

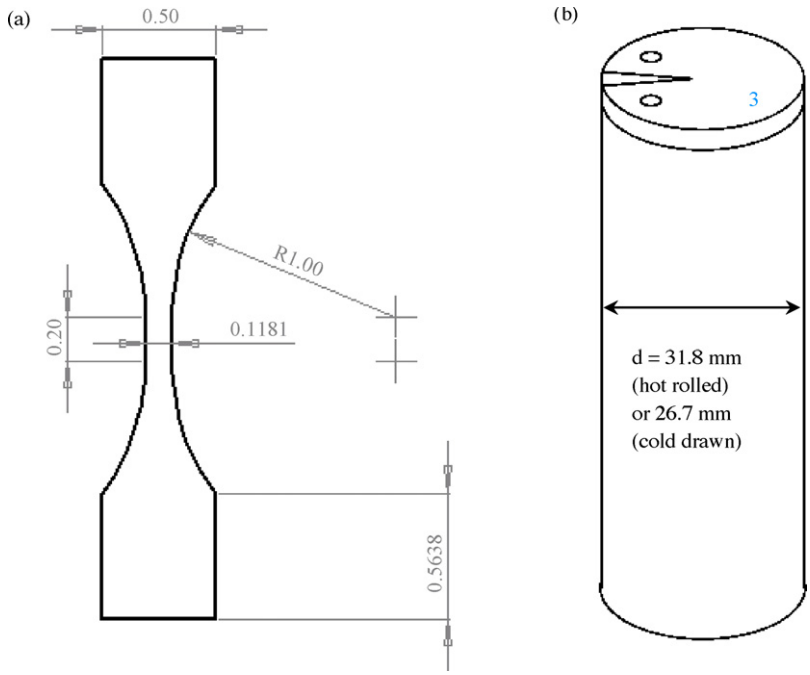

Fig. 1. Specimen geometries for (a) monotonic and cyclic tensile testing with dimensions in inches and (b) fatigue crack growth testing. The tensile specimens in (a) were all extracted with the loading axis parallel to the rolling or drawing direction.

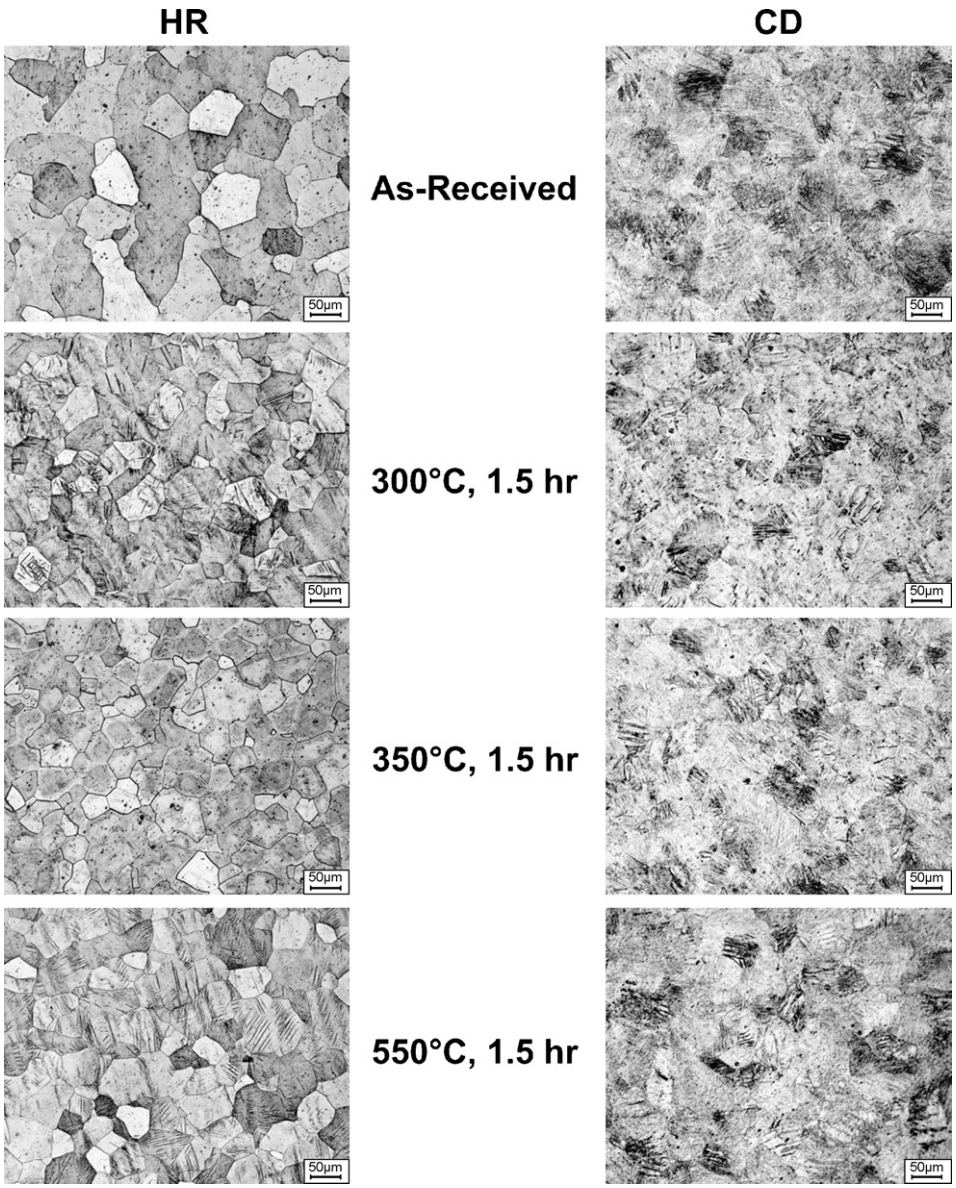

Fig. 2. Optical micrographs of Nitinol hot-rolled (HR) and cold-drawn (CD) bar. Hot-rolled and cold-drawn bars show nearly equal grain sizes regardless of heat treatment, specifically 74 μm and 60 μm, respectively [65,73]. All surfaces were electropolished followed by chemical etching to reveal the microstructure (etchant: 3.2% HF, 14.6% HNO_3, balance deionized water). The rolling direction is out-of-plane in each micrograph (i.e., transverse cross-section). Note the presence of martensite in all of the cold-drawn materials, as indicated by their lathe microstructure, suggesting higher residual strains than the hot-rolled materials.

ing/rolling direction, and grain sizes in the 60–70 μm range [65,73] (Fig. 2). As expected the cold-drawn material has slightly smaller average transverse grain size (60 μm) compared to the hot-rolled material (average grain size of 74 μm) [65]. On an area basis, this difference is consistent with the 30% reduction given to the hot-rolled material to create the cold-drawn material [65]. In addition, the ⟨1 1 1⟩ fiber texture is slightly stronger in the cold-drawn material compared to the hot-rolled material.

TEM images of the material microstructures as a function of heat treatment are presented in Figs. 3 and 4 for the hot-rolled and cold-drawn materials, respectively. The as-received hot-rolled material is nearly fully solutionized with only a very fine distribution of precipitates (Fig. 3a). Aging at either 300 °C or 350 °C results in a more noticeable distribution of fine precipitates (10 nm size range) in both materials, Fig. 3b and c, respectively. Aging at 550 °C results in an overaged state with relatively large incoherent precipitates of several hundreds of nanometers in size.

The as-received cold-drawn material is a complicated mixture of dislocations and residual martensite induced during the cold drawing of the hot-rolled bar (Fig. 4a). Aging at 300 °C or 350 °C does not cause measurable changes in material structure through representative TEM images (Fig. 4b and c). The materials aged at 300 °C and 350 °C both contain a high dislocation density and residual martensite laths, even though the high magnification in Fig. 4c highlights the dislocation arrangement. Aging the cold-drawn material at 550 °C results in recovery, recrystallization, and grain growth, as shown in Fig. 4d. Precipitates were not distinguishable in the cold-drawn materials due to the defect-laden microstructure. However, the trends in hardness with heat

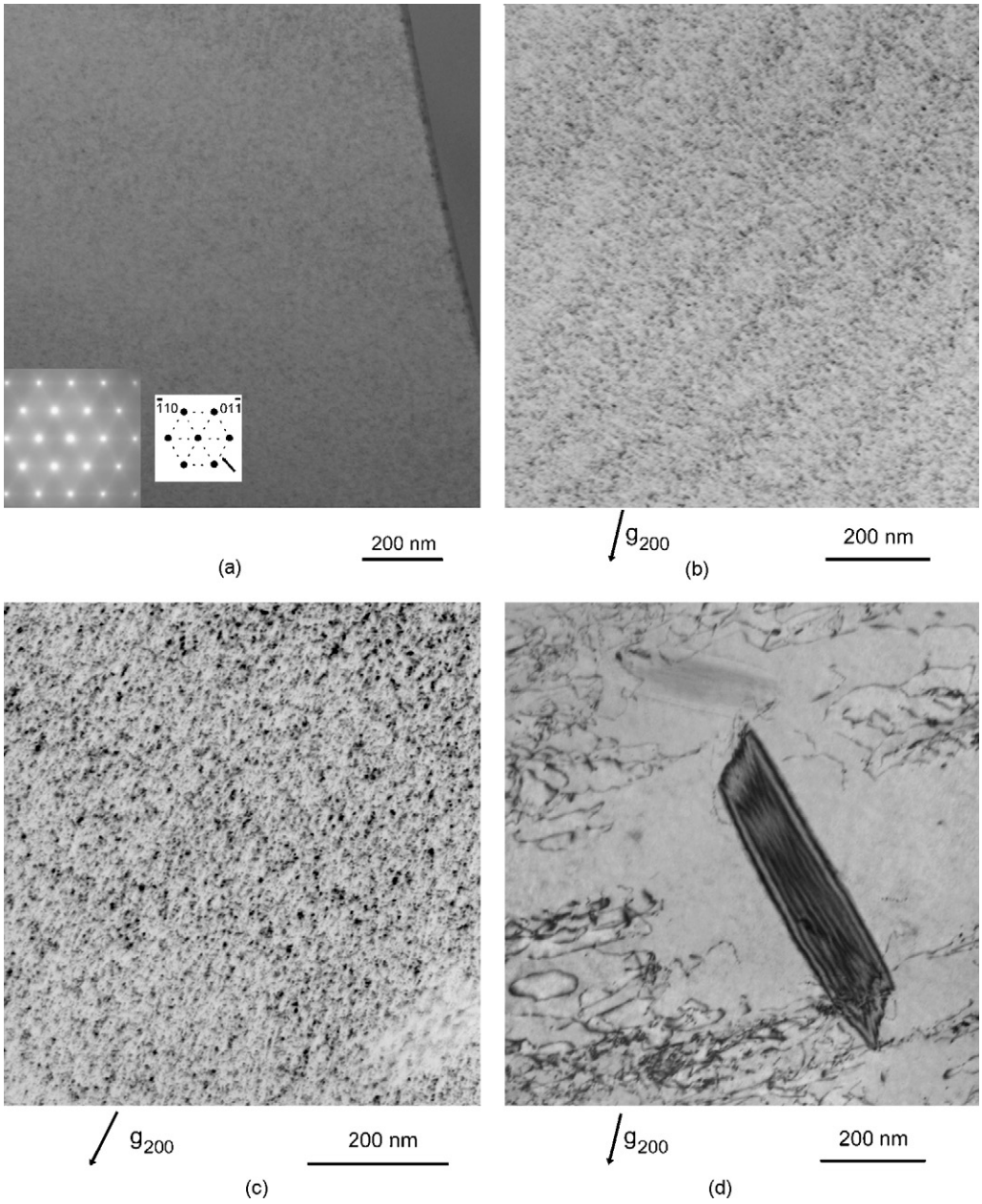

Fig. 3. Transmission electron microscopy images for the hot-rolled and annealed NiTi: (a) as-received [65], (b) 300 °C for 1.5 h, (c) 350 °C for 1.5 h, and (d) 550 °C for 1.5 h.

treatment presented herein, and prior TEM work [73], would imply activation of precipitation hardening.

3.2. Thermal transformation

Here we provide a summary of thermal transformation behavior for the hot-rolled and cold-drawn materials as a function of heat treatment. More details on the interpretation of specific transformation peaks can be found in Ref. [73].

Thermal transformation behavior as a function of heat treatment is shown in Fig. 5 for the (a) hot-rolled and (b) cold-drawn materials. The as-received hot-rolled material undergoes a single step transformation from austenite to martensite upon cooling and from martensite to austenite upon heating. Heat treatment at 300 °C or 350 °C brings out a multi-step R-phase transformation (one signature of a precipitated microstructure) and also changes the position of the primary martensite start and finish temperatures. Aging at 550 °C results in a considerable change in transformation behavior with a two-step transformation upon cooling and a single-step transformation during heating. The thermal transformation behavior of the as-received hot-rolled material and the hot-rolled material aged at 550 °C are only slightly different in terms of temperature location and transformation sequence.

The as-received cold-drawn material does not show any detectable transformation peaks in the temperature range considered (Fig. 5b). Aging at 300 °C and 350 °C brings out a subtle R-phase transformation (Fig. 5b) at temperatures very close to

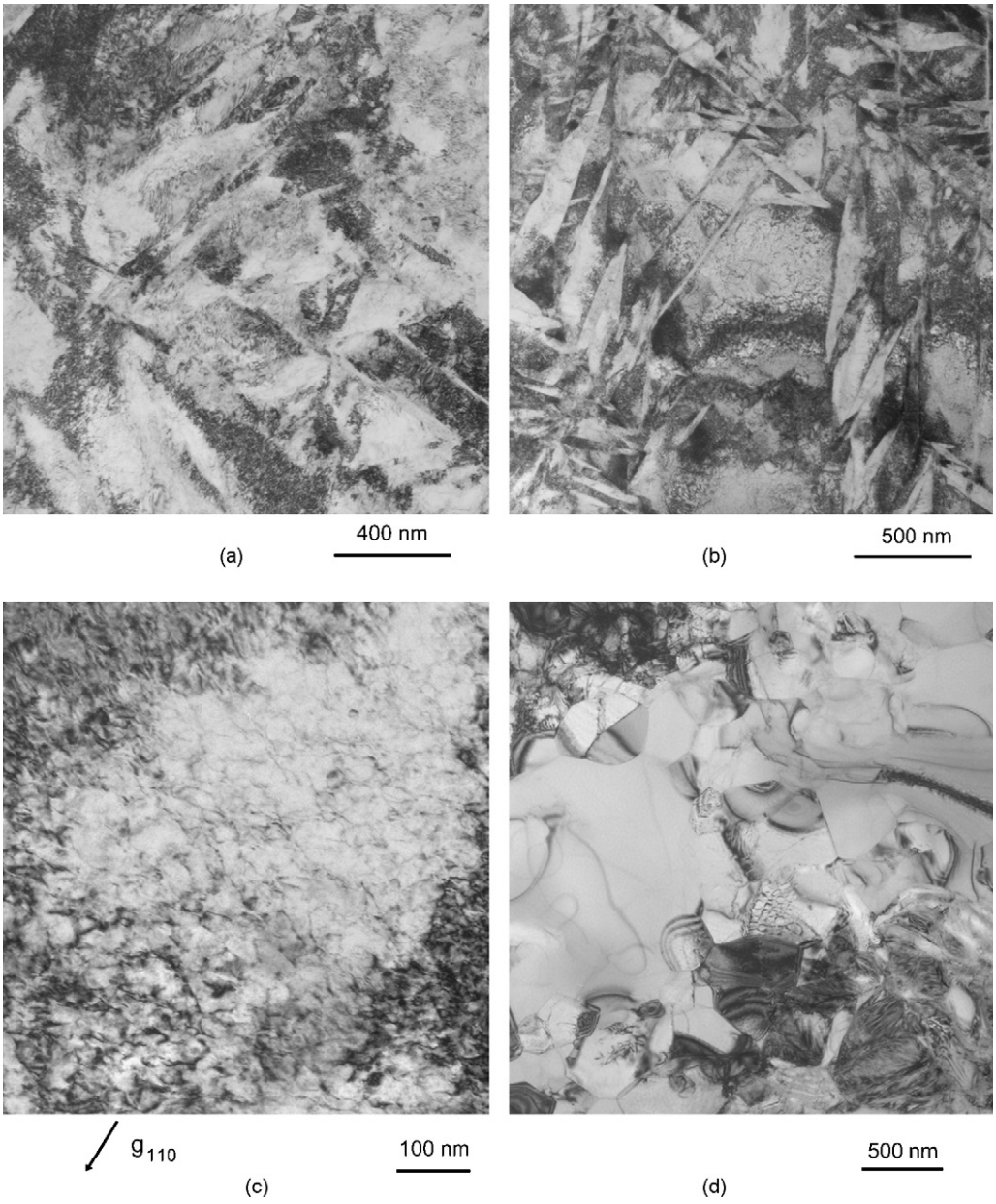

Fig. 4. Transmission electron microscopy images for the cold-drawn and annealed NiTi: (a) as-received [73], (b) 300 °C for 1.5 h, (c) 350 °C for 1.5 h, and (d) 550 °C for 1.5 h.

the clear R-phase peaks in the hot-rolled material (Fig. 5a). The primary martensitic transformation is not detectable through DSC in the mildly aged cold-drawn materials. Aging the cold-drawn material at 550 °C results in the appearance of the primary martensitic transformation and occurrence of a multi-step phase transformation in similar temperature vicinity as the hot-rolled material.

3.3. Hardness

Hardness tests were performed to help assist interpretation of material microstructure as a function of heat treatment, and provide a simple metric for potential correlation with results from monotonic and cyclic tests. Fig. 6 presents hardness trends in the hot-rolled and cold-drawn materials as a function of heat treatment. The error bars represent one standard deviation in the measurements, and experimental scatter was typically very low. The as-received cold-drawn material is considerably harder than the as-received hot-rolled material, consistent with the relatively high density of defects induced by cold drawing, and observed in TEM. At a heat treatment temperature of 300 °C, both materials experience a 5–15% increase in hardness. The increase in hardness in the hot-rolled material is due to a precipitation hardening effect (Fig. 3b). Although precipitates were not detectable by TEM in the cold-drawn material (Fig. 4b), it is reasonable to expect some precipitation hardening since the Ni-rich hot-rolled material is the precursor to the cold-drawn material, and Ni is not lost during the cold-drawing process. In addition, prior work has observed evidence of precipitates in the cold-drawn material [73]. Aging both materials at a slightly higher temper-

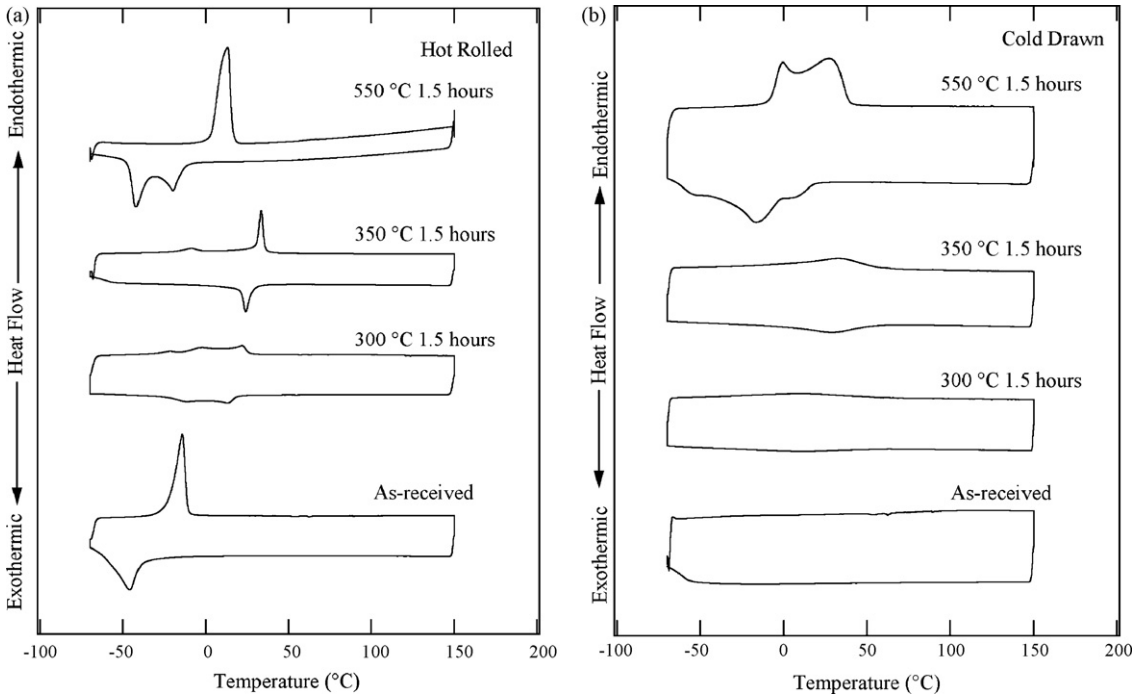

Fig. 5. Differential scanning calorimetry curves for the (a) hot-rolled and (b) cold-drawn materials as a function of heat treatment. Measured A_f temperatures are presented in Table 2.

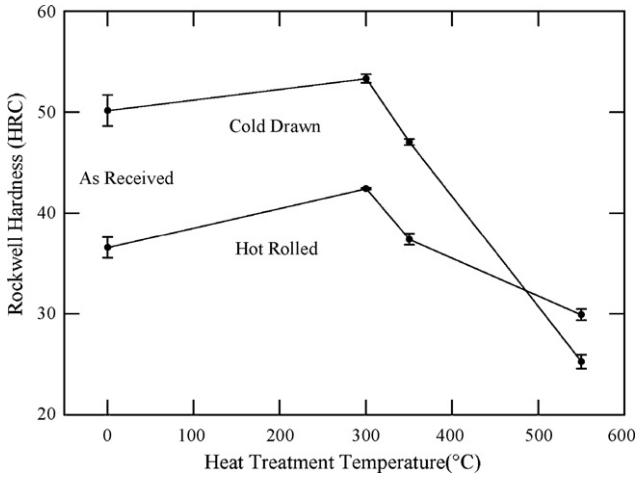

Fig. 6. Hardness (HRC) as a function of heat treatment and deformation processing.

ature (350 °C) results in a consistent drop in hardness (∼12%). Finally, when the hot-rolled and cold-drawn materials are aged at 550 °C, both materials experience a more significant drop in hardness, consistent with the large precipitate structure in the hot-rolled materials (Fig. 3d) and the recovered structure in the cold-drawn material (Fig. 4d).

3.4. Monotonic stress–strain response

We have performed stress–strain tests at both ambient temperature (25 °C) and elevated temperatures (125 °C or 150 °C). The monotonic tests provide common ground in order to better understand the link between cyclic tests and material structure. Stress–strain curves for the hot-rolled material at (a) ambient and (b) elevated temperature are presented in Fig. 7. At ambient temperature (Fig. 7a) the initial portion of the stress–strain curve characterizes the stress-induced transformation and can be linked to DSC results, while the latter stages of the stress–strain

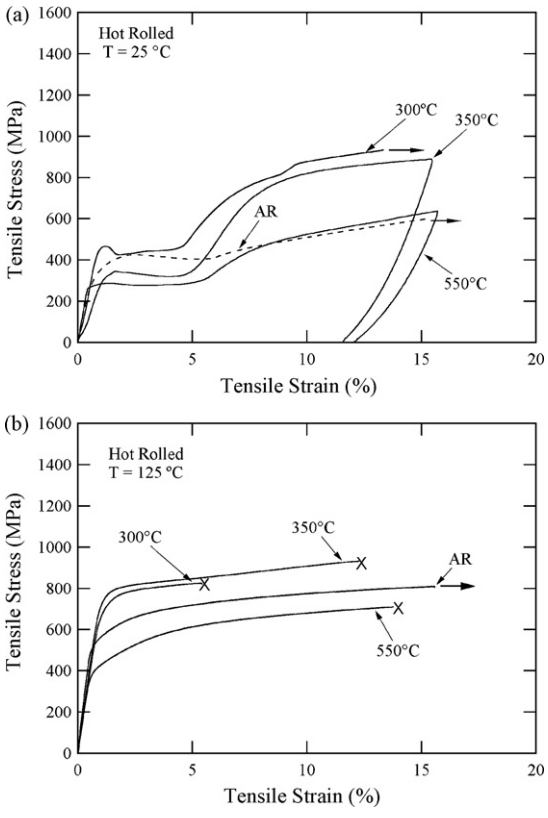

Fig. 7. Monotonic stress–strain response of the hot-rolled NiTi specimens tested at (a) ambient (25 °C) and (b) elevated (125 °C) temperatures.

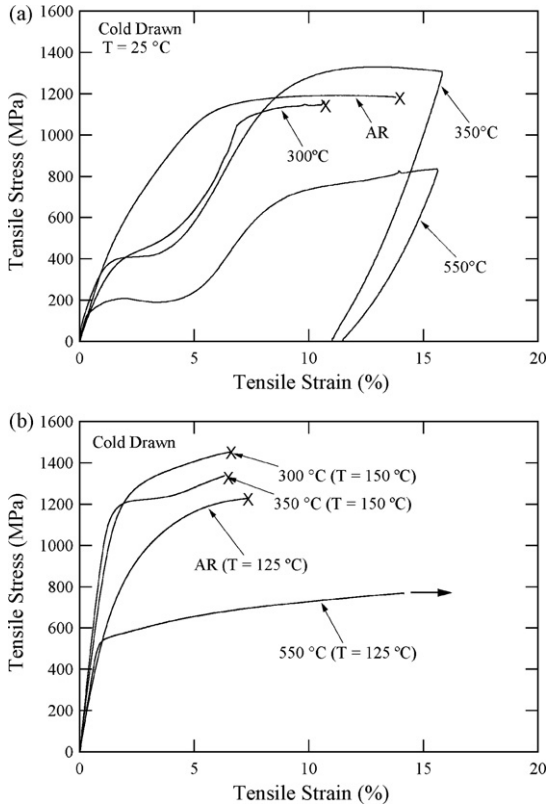

Fig. 8. Monotonic stress–strain response of the cold-drawn NiTi specimens tested at (a) ambient (25 °C) and (b) elevated (125 and 150 °C) temperatures.

curve characterize yield and plastic flow of the martensite and can be linked to hardness results. The critical transformation stress in the hot-rolled material decreases with increasing aging temperature, consistent with increasing transformation temperatures observed in DSC. The flow strength of the stress-induced martensite (for example, the stress at ∼10% strain after the second "yield") also decreases with increasing aging temperature, a result consistent with hardness testing.

The elevated temperature response above M_d (Fig. 7b) was measured to characterize the elastic–plastic flow behavior of the transformation-suppressed austenite phase of the material. The elevated temperature results show similar trends as the large-strain ambient temperature results and the hardness tests. Specifically, the austenite flow strength is the highest for the materials heat treated to 300 °C and 350 °C, while the as-received material and material aged at 550 °C are consistently weaker.

Stress–strain curves for the cold-drawn material at (a) ambient and (b) elevated temperature are presented in Fig. 8. The as-received cold-drawn material demonstrates only plastic flow, with no evidence of a stress-induced transformation at either testing temperature. At ambient temperature (Fig. 8a), the cold-drawn materials heat treated at 300 °C and 350 °C show similar response with critical transformation stress levels similar to those in the mildly aged hot-rolled materials but martensite flow strengths ∼30% higher. Aging the cold-drawn material at 550 °C results in a considerable drop in the transformation stress and martensite flow strength. We mention here that the elastic modulus of the material apparently varies with heat treatment. However, this variation is more indicative of issues with inelastic contribution to the elastic loading regime where relative proximity to a transformation temperature can alter what appears to be an elastic loading regime [65].

The elevated temperature tests (Fig. 8b) on the cold-drawn materials reveal similar trends for the austenite flow strength as a function of heat treatment compared to the martensite flow strength. The changes in the austenite and martensite flow strength of the cold-drawn material follow trends in hardness as a function of heat treatment. Moreover, the strength levels in both the hot-rolled and cold-drawn materials are consistent with changes in microstructure observed with TEM as a function of heat treatment. Specifically, these results support the conclusion of precipitation hardening in the hot-rolled material and precipitation hardening plus dislocation hardening in the cold-drawn material.

3.5. Low-cycle fatigue tests

Low-cycle pseudoelastic fatigue tests were performed to gain insight into the effect of heat treatment and microstructure, with each cycle characterized by a forward loading from 0 MPa to 3% tensile strain, and reverse loading back to 0 MPa. The data are presented as a series of selected cyclic stress–strain curves, over 100 cycles, aimed at assessing cyclic stability of the various materials. The representative cyclic data for the as-received, aged 300 °C, aged 350 °C, and aged 550 °C specimens are shown, respectively, in Figs. 9–12 for a cyclic strain range of 3%.

Since the cold-drawn material did not transform in the as-received state, we only performed tests on the as-received hot-rolled material (Fig. 9). Materials with poor cyclic stability show appreciable accumulation of permanent strain and significant changes in hysteresis loop shape with cycling. The as-received hot-rolled material demonstrates both cyclic unrecoverable strains and significant change in the hysteresis of the stress–strain curve during cycling (Fig. 9).

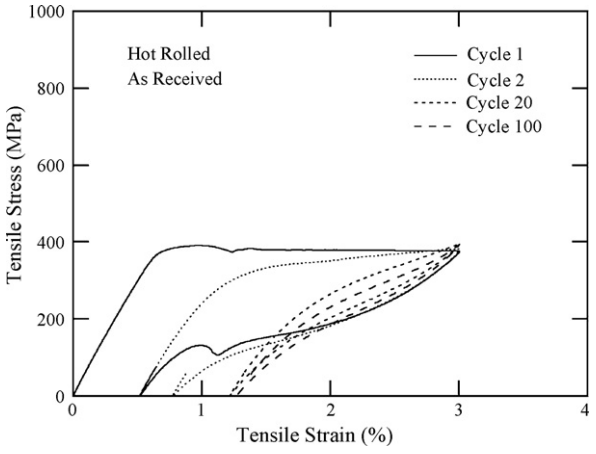

Fig. 9. Tensile low-cycle fatigue response of the as-received hot-rolled material. The as-received cold-drawn material was not tested because it demonstrates only permanent plastic strains whereas the as-received hot-rolled material exhibits a reversible transformation.

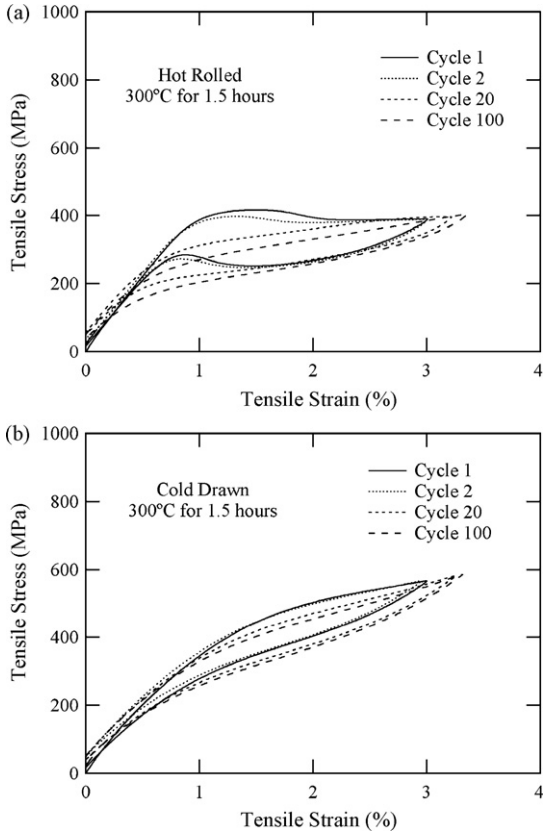

Fig. 10. Tensile low-cycle fatigue response of the (a) hot-rolled and (b) cold-drawn materials aged at 300 °C for 1.5 h.

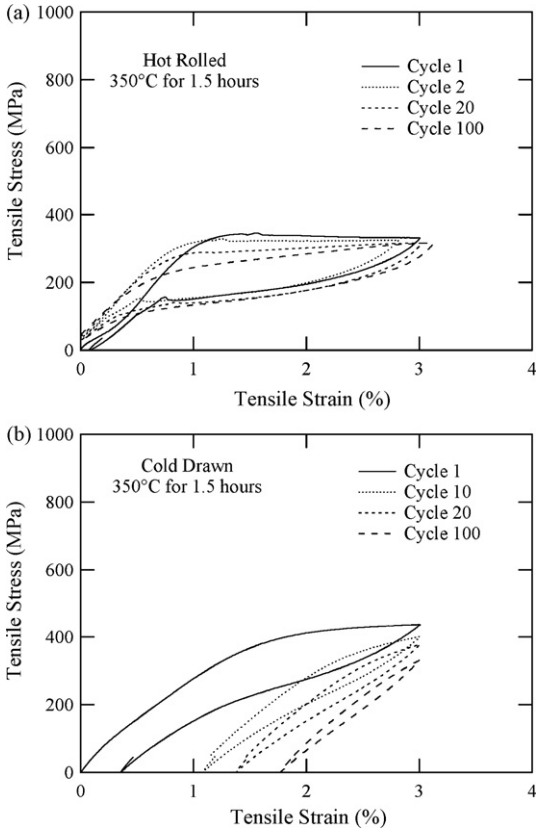

Fig. 11. Tensile low-cycle fatigue response of the (a) hot-rolled and (b) cold-drawn materials aged at 350 °C for 1.5 h.

The cyclic response of (a) the hot-rolled and (b) cold-drawn materials aged 300 °C are shown in Fig. 10. Neither material showed appreciable unrecoverable strain as a function of cycling. The hot-rolled material demonstrated larger changes in the shape of the pseudoelastic loop versus cycling of the cold-drawn material. In fact, at 100 cycles, the overall shapes of the stress–strain curves for the two materials appeared similar. Both materials possessed much improved cyclic stability compared to the as-received hot-rolled material, which demonstrated considerable unrecoverable cyclic strain.

The materials aged at 350 °C exhibited a much different and repeatable cyclic response (Fig. 11). The hot-rolled material still demonstrated excellent cyclic stability (Fig. 11a), while the cold-drawn material showed relatively poor cyclic properties with considerable unrecoverable strain and hysteresis loop closure (Fig. 11b). The trends in cyclic behavior at 3% strain range were repeated for the materials aged at 300 °C and 350 °C for the hot-rolled and cold-drawn materials with a strain range of 6%. For a 6% strain amplitude, the trends were identical with excellent cyclic degradation resistance in the hot-rolled and cold-drawn materials aged at 300 °C and hot-rolled material aged at 350 °C. The cold-drawn material aged at 350 °C showed the worst resistance to cyclic degradation.

Finally, the cyclic stress–strain data from the materials aged at 550 °C is shown in Fig. 12. The hot-rolled and cold-drawn materials both show poor cyclic stability under the imposed test conditions because both materials have *very* low-strength microstructures that are ineffective in preventing dislocation motion while promoting the transformation, resulting in rapid cyclic degradation.

At first glance, the improved low-cycle fatigue response of the 300 °C aged (vs. as-received) samples can be explained by the higher hardness and flow strength in response to the aging. Clearly, the improved mechanical flow properties of the two materials are contributing to the increased resistance to pseudoelastic fatigue since the dislocation motion resistant structures favor fully reversible transformation rather than permanent deformation. However, the cyclic results for the materials heat treated at 350 °C (Fig. 11) highlight the limitation of this argument, especially when comparing across material systems (hot-rolled vs. cold-drawn). Indeed, the transformation stresses in both the hot-rolled and cold-drawn 350 °C specimens were similar and less than that of the 300 °C aged materials, eliminating applied stress or vicinity to the transformation temperatures as a plausible explanation. Furthermore, *all* monotonic measures (hardness, austenite flow strength, and martensite flow strength) show that the resistance to plastic flow of the cold-drawn material aged at 350 °C is significantly higher than that of the hot-rolled material aged at 350 °C, indicating that one cannot use monotonic strength measures alone to optimize the low-cycle fatigue resistance in NiTi when considering different processing routes. It should explicitly be pointed out that this work reveals the importance of selecting "optimal" heat treatments based on the specific processing route, hot-rolled versus

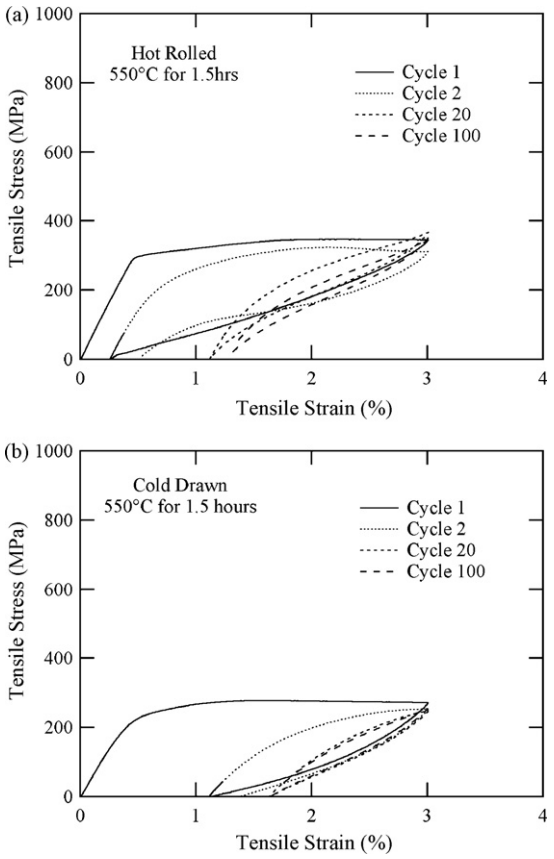

Fig. 12. Tensile low-cycle fatigue response of the (a) hot-rolled and (b) cold-drawn materials aged at 550 °C for 1.5 h.

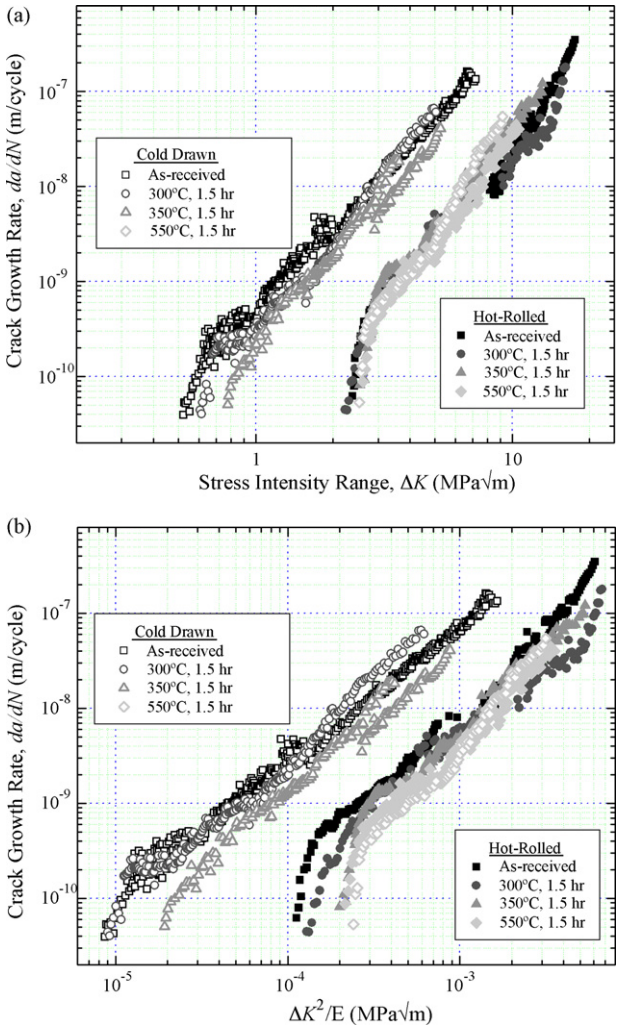

Fig. 13. Fatigue crack growth plots: (a) fatigue crack growth rates, d*a*/d*N*, as a function of the stress intensity range, Δ*K*, showing marked differences in behavior of the cold-drawn (except after annealing at 550 °C) and hot-rolled material and (b) crack growth rates plotted against stress intensity range normalized by the elastic modulus *E*, which reveal little convergence of the data.

cold-drawn or cold-drawn wires versus cold-drawn bars. In addition, the treatment that optimizes one property may not optimize or even influence another property. For example, prior work has suggested ideal heat treatments for NiTi wires following cold working [31]. Although these treatments may be optimal for the specific composition, product form, and reduction, they are not necessarily the optimal heat treatment across all material variations as demonstrated herein.

3.6. Fatigue crack growth behavior

In addition to resistance to low-cycle pseudoelastic fatigue, NiTi often is required in engineering applications to resist high cycle, low amplitude fatigue. We have performed a series of fatigue crack growth experiments to better understand the effect of material form and microstructure on such high-cycle fatigue behavior. Fig. 13 graphically shows, and Table 1 quantifies, the threshold ΔK_{th} values for each condition. A standard represen-

Table 1
Fatigue crack growth properties of heat-treated Nitinol bar

Processing	Heat treatment	Fatigue threshold, ΔK_{th} (MPa$\sqrt{m}$)	Paris-law exponents		ΔCTOD (nm)	$CTOD_{Max}$ (nm)
			m	C (m/(cycle (MPa$\sqrt{m}$)^m))		
Hot-rolled	As-received	2.46	3.32	1.25×10^{-11}	28.9	71.4
	300 °C, 1.5 h	2.42	2.76	3.32×10^{-11}	56.6	139
	350 °C, 1.5 h	2.62	3.66	9.62×10^{-12}	58.4	144
	550 °C, 1.5 h	2.68	3.46	1.02×10^{-11}	28.8	71.1
Cold-drawn	As-received	0.581	2.79	5.68×10^{-10}	0.73	1.80
	300 °C, 1.5 h	0.650	3.30	2.77×10^{-10}	1.60	3.96
	350 °C, 1.5 h	0.833	3.05	2.36×10^{-10}	0.95	2.34
	550 °C, 1.5 h	2.57	4.14	4.66×10^{-12}	45.6	113

Table 2
Material properties of Nitinol bar

Processing	Heat treatment	A_f (°C)	Tensile properties[a]		Residual strain	
			Elastic modulus (GPa)	Yield stress (MPa)	FWHM (milli-rad)	FWHM/FWHM$_{HR550}$
Hot-rolled	As-received	50	50.6	228	0.80	0.7
	300 °C, 1.5 h	30	38.7	246	1.24	1.1
	350 °C, 1.5 h	39	32.2	233	2.23	2.0
	550 °C, 1.5 h	15	61.8	185	1.10	1.0
Cold-drawn	As-received	0	31.4	605	7.47	7.0
	300 °C, 1.5 h	−5	41.0	304	8.11	7.4
	350 °C, 1.5 h	63	31.4	350	8.04	7.3
	550 °C, 1.5 h	20	26.7	205	1.90	1.7

[a] Tensile properties determined from stress–strain plots at the 100th fatigue cycle such that steady state was reached.

tation of crack growth rates plotted as a function of the stress intensity range is presented in Fig. 13a and shows a clear distinction between the hot-rolled and the cold-drawn materials. All four of the hot-rolled annealing conditions produced nominally the same fatigue crack growth properties. Conversely, the cold-drawn material demonstrated the lowest threshold ΔK_{th} values in the as-received condition ($\Delta K_{th} \sim 0.6\,\mathrm{MPa}\sqrt{\mathrm{m}}$, which is some 2–25 times lower than any other metallic alloy [74,75]), with the threshold values increasing with a corresponding increase in annealing temperature, finally culminating in the cold-drawn 550 °C material demonstrating fatigue crack growth properties nearly identical to its hot-rolled

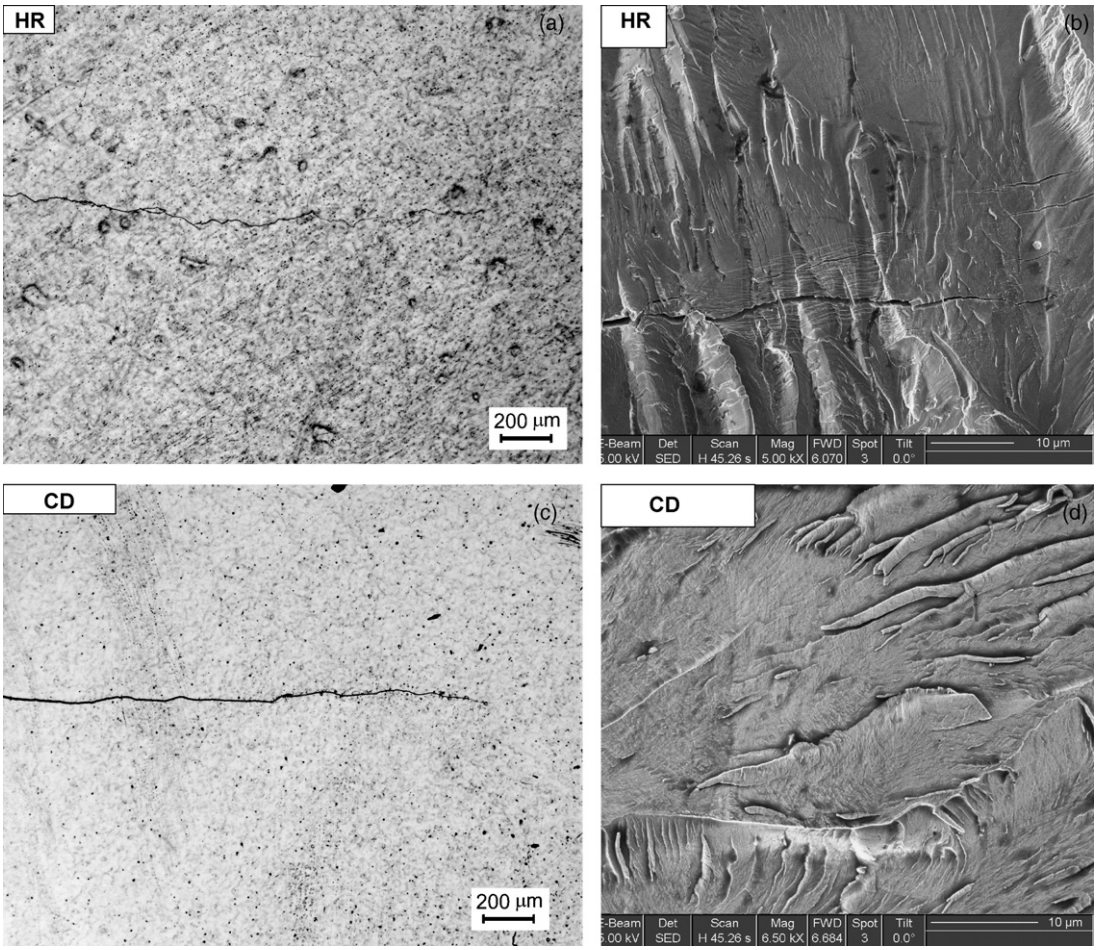

Fig. 14. The morphology of fatigue crack paths and fracture surfaces in the as-received NiTi material. (a) A cross-sectional view of the fatigue crack path in the hot-rolled material showing crack surface asperities with a nominal height of ~35 μm; (b) a corresponding scanning electron microscopy image of the fatigue fracture surface showing significant secondary microcracking at near-threshold levels ($da/dN \sim 10^{-10}$ m/cycle, $\Delta K \sim 2.6\,\mathrm{MPa}\sqrt{\mathrm{m}}$); (c) a cross-sectional view of the crack path in the cold-drawn material showing minimal crack deflection and much smaller asperities (height ~10 μm); (d) a corresponding image of the fracture surface which shows a relatively smooth, quasi-cleavage-like appearance ($da/dN \sim 10^{-10}$ m/cycle, $\Delta K \sim 0.6\,\mathrm{MPa}\sqrt{\mathrm{m}}$). All micrographs show the crack growing from left to right.

counterparts ($\Delta K_{th} \sim 2.5\,MPa\sqrt{m}$). Fatigue thresholds intensities of this magnitude ($\Delta K_{th} \sim 2.5\,MPa\sqrt{m}$) are typical for other NiTi materials reported in the literature [46,47,49–52,70], which range from $2\,MPa\sqrt{m}$ to $4\,MPa\sqrt{m}$ at this low load ratio.

The basic mechanical properties (elastic modulus and yield strength) of the NiTi bars are drastically influenced by the heat treatments. Table 2 presents the elastic modulus and 0.2% offset transformation stress determined following 100 fatigue cycles (from Figs. 9–12) to allow stabilization of the linear-elastic response due to martensite stabilization. The hot-rolled material yield stresses remain relatively unchanged with heat treatment; however, the cycle-stabilized elastic modulus at ambient temperature varied significantly. Conversely, the cold-drawn material (except for the 300 °C, 1.5 h treatment) shows relatively stable moduli with varying yield stress. However, there is not a clear trend in these elastic material properties that can explain the differences in fatigue behavior. Indeed, often times fatigue crack growth behavior from many different materials can be normalized by plotting the data as a function of the stress intensity range divided by the elastic (Young's) modulus, E, of the material, rather than direct comparison to the ΔK. This follows because crack growth rates can often be related to the crack opening displacement per cycle, which is a function of $\Delta K^2/E$. However, Fig. 13b clearly shows that the current results cannot be effectively normalized by the elastic modulus, suggesting that the observed differences in fatigue behavior are not associated with variations in the mechanical properties of the materials, but instead by microstructural factors.

Although less important than the fatigue threshold for controlling the fatigue life of physically small devices, such as stents, the Paris-law crack growth exponent, m, and scaling constant, C, are important in lifetime predictions for larger structures (e.g., earthquake reinforcement structures [76–78]), which can withstand a certain amount of crack growth without imminent threat of failure. These values may be used to conservatively estimate the lifetime of a NiTi device with a known maximum flaw size, by integrating the Paris law: $da/dN = C\Delta K^m$, where da/dN is the measure of crack propagation per fatigue cycle and ΔK is the stress intensity range. Compared to previous work in NiTi bar [46,47,49], growth rates in the present alloys are somewhat faster (crack growth exponents are $m \sim 3$–4, as compared to ~2–3 in bar), and approximately the same when compared to deep-drawn NiTi tube [51,52].

Fig. 14 presents optical and scanning electron micrographs of the fracture cross-sections and surfaces taken at near-threshold stress intensities in the hot-rolled and cold-drawn as-received specimens. It is apparent that the size of asperities on the crack surfaces (which often is an effective source of fatigue crack closure [79]) are much larger in the hot-rolled material (Fig. 14a) when compared to the cold-drawn material (Fig. 14c); this is most likely due to the difference in grain sizes, with the hot-rolled material exhibiting ~25% larger average grain sizes. Secondary microcracking was also observed in the propagating fatigue front in the hot-rolled as-received specimen (Fig. 14b). The formation of secondary microcracks acts as an energy dissipating mechanism and can partially explain the higher fatigue threshold values in the hot-rolled material. The cold-drawn material exhibited quasi-cleavage type fracture typical in brittle materials (Fig. 14d).

Crack tip opening displacements (CTOD) were calculated [80] for each threshold condition and were based upon the 0.2% offset yield value at the 100th fatigue cycle presented in Table 1.[1] As expected, due to the low fatigue thresholds, the cold-drawn materials (except at 550 °C) had extremely small ΔCTOD values because of the proportionality to the threshold stress intensity. Those opening displacements were 1.60 nm or less, which is ~1/10 of the native oxide thickness for this material [81], suggesting that the presence of a fatigue threshold (although low) in the cold-drawn material were most likely associated with crack wedging by the oxide film and fracture surface asperities in the vicinity of the crack tip; the existence of such crack closure lowers the effective (local) stress intensity range by effectively raising the minimum stress intensity in the cycle. Conversely, the hot-rolled and the cold-drawn (550 °C) specimens had ΔCTOD values 3–5 times the native oxide thickness, but still smaller than the asperity heights, indicating that wedging effects from the oxide were highly unlikely, but frictional dissipation of energy due to grain-to-grain interference could not be ruled out as the source of the asymptotic fatigue threshold.

As the fatigue test specimens were prepared, and test conditions designed, such that there were no physical (e.g., surface roughness) or mechanical (e.g., plane stress vs. strain) differences between specimens, it is reasonable to attribute the observed differences in the fatigue behavior to one or more internal "material" properties that are unique to each specimen; these are compared in Table 2. As discussed earlier, there was no correlation between the elastic modulus and the fatigue resistance. Furthermore, there was no observed correlation to the yield stress or to the transformation (A_f) temperature, which indicated that all tests were conducted in the austenite phase or mixed austenite/R-phase. Moreover, the difference in grain sizes, i.e., 75 μm in hot-rolled versus in 60 μm cold-drawn material (Fig. 2), was relatively small, and although crack closure from interference of wedging grains in the wake of a fatigue crack certainly can influence the fatigue crack growth and threshold properties, these effects cannot explain the extremely low values of the fatigue threshold in the hot-rolled material and cold-drawn material.

The most significant difference between the eight samples was the residual strain in each sample, which is processing-based rather than a material property, but is an unavoidable result of the cold drawing. Uniform strain due to elastic response of the polycrystals, and non-uniform strain attributed to lattice accommodation of dislocation packets, inclusions, or precipitates in the material can be measured by differences in X-ray diffraction (XRD) patterns. Specifically, we chose to quantify the residual strains in the material by measuring peak broadening via a full

[1] Crack tip opening displacements were calculated from Ref. [80] using the relationships: $\Delta CTOD_{th} = d_n \Delta K_{th}/2\sigma_y E$, $CTOD_{max,th} = d_n K_{max,th}/\sigma_y E$ where d_n is a dimensionless parameter, ranging in value from 0.3 to 1.0, which is a function of the yield strain, the work hardening exponent, and whether plane stress or plane strain conditions are assumed.

width at half maximum (FWHM) calculation at the 1 1 0 diffraction peak. The FWHM values (measured in milli-radian of peak broadening) are presented in Table 2, and clearly demonstrate that the cold-drawn samples (excluding the 550 °C annealing condition) have a much broader peak, implying higher residual strain, consistent with the higher dislocation density observed by TEM. Normalizing those results with the sample that should contain the least residual stress (i.e., hot-rolled 550 °C annealing condition, which we term the "reference" sample) resulted in an excellent qualitative correlation to the fatigue crack growth results. Samples that exhibited the higher fatigue threshold values (cold drawn, annealed at 550 °C) had FWHM values equal to, or below, twice the "reference" condition (i.e., lower residual stress), whereas the specimens with low threshold values (cold drawn, all but 550 °C) had over seven times the peak width when compared to the "reference" condition (i.e., they possessed much higher residual stresses).

To highlight the extent to which such residual stresses can distort the measured fatigue thresholds, we compared the fatigue crack growth properties of these NiTi alloys to several other materials that are used for other biomedical implants (Fig. 15a), namely, pyrolytic carbon [82], NiTi tube [51,52], L605 (CoCr alloy) [83], Ti–6Al–4V, and 316 stainless steel [47]. Although the hot-rolled NiTi bar shows fatigue thresholds similar to commercial NiTi tube, surprisingly cold-drawn (as-received) NiTi bar has the lowest fatigue threshold of any of these materials, including the brittle ceramic-like pyrolytic carbon material. Therefore, the design of any product manufactured from cold-drawn bar (except after annealing at higher (550 °C) temperatures) will require enhanced scrutiny of components as extremely small flaw sizes will need to be detected in order to prevent the growth of fatigue cracks.

Normalization of the fatigue crack growth curves by the elastic modulus (Fig. 15b) did produce some convergence of the growth curves, with all of the ΔK_{th} values falling within a single logarithmic decade; however, the cold-drawn as-received material still exhibited the lowest fatigue threshold.

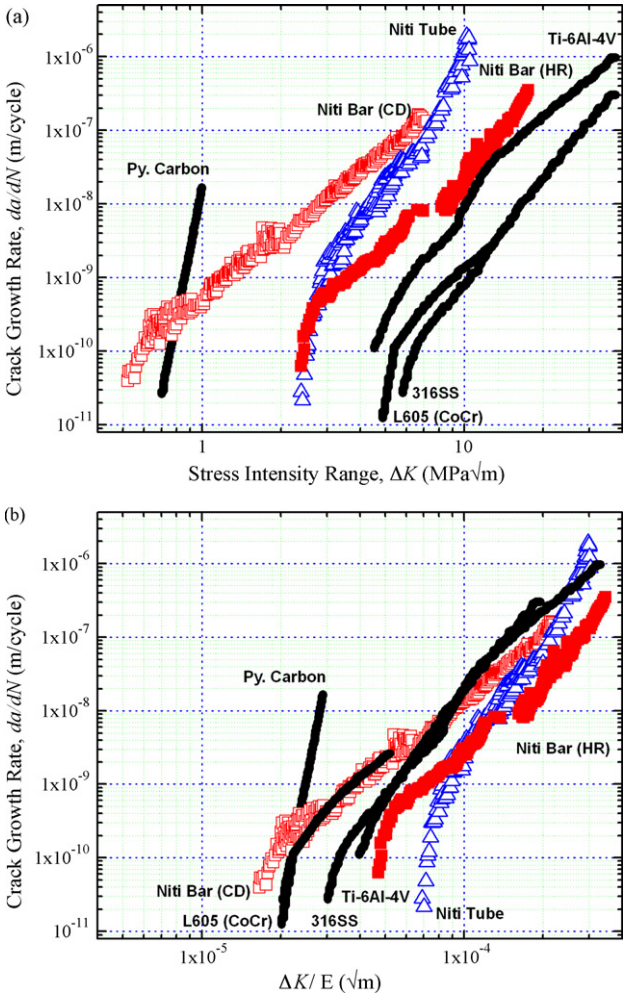

Fig. 15. A comparison of fatigue crack growth properties of the current NiTi alloys with other materials commonly used for biomedical implants: (a) fatigue crack growth rate behavior plotted as a function of the stress intensity range, ΔK (the as-received Nitinol bars tested in the current work are shown in red, Nitinol tube [51,52] in blue, and other biomaterials in black) and (b) the same crack growth rate behavior normalized by $\Delta K/E$, where E is the elastic modulus (this shows some degree of normalization of the data to within a single logarithmic decade). Note that the cold-drawn as-received material has a fatigue threshold ΔK_{th} value significantly lower than other implant materials, including the ceramic-like pyrolytic carbon. (For interpretation of the references to color in this figure legend, the reader is referred to the web version of the article.)

4. Summary and conclusions

In-service fatigue of NiTi components, particularly biomedical implant devices such as endovascular stents, can be extremely complex since the material can experience combinations of low-cycle and high-cycle fatigue loading, and mixed-mode loads from tension, compression, bending and shear. In order to appropriately design devices from NiTi shape memory alloys, it is imperative to understand processing–structure–property relationships under cyclic loading conditions. Such information allows tailoring of material processing and structure to achieve optimized resistance against fatigue failure. Prior work has established basic relationships between fatigue properties and processing parameters; however, this understanding is insufficient to truly optimize fatigue resistance under all microstructural conditions. The present work provides a further foundation to better understand the fatigue resistance of NiTi shape memory alloys. Specific conclusions include:

(1) Increases in monotonic strength measures in both the hot-rolled and cold-drawn NiTi materials leads to enhanced resistance to low-cycle fatigue (increased pseudoelastic stability) as long as the primary material processing route remains unchanged.
(2) An increase in material "flow strength" is a necessary, but not always sufficient, means to improve resistance to cyclic pseudoelastic degradation. It is possible to have a relatively high-strength material that undergoes the transformation, but exhibits poor cyclic stability relative to a lower-strength NiTi material, especially when considering different primary processing routes.
(3) The hot-rolled material exhibited fatigue crack growth behavior similar to other reports of superelastic NiTi in the

literature with a fatigue threshold of ~2.5 MPa$\sqrt{m}$ regardless of the aging treatment.

(4) The cold-drawn as-received material exhibits threshold values of ~0.6 MPa$\sqrt{m}$, which is lower than most materials used for biomedical applications, including brittle pyrolytic carbon, and is indeed some 2 to 25 times lower than any other metallic material.

(5) The extremely low fatigue threshold in the cold-drawn bar is attributed to residual stresses imparted in the NiTi material during the cold-drawing process. Reduction of residual stresses in this material using annealing processes results in a corresponding increase in fatigue crack growth resistance.

Acknowledgements

This work was supported by a PECASE award and the Coleman Institute (for KG, JT, and GW), and by the National Science Foundation under grant number CMS-0409294 (for SWR and ROR).

References

[1] S.A. Shabalovskaya, Bio-Med. Mater. Eng. 6 (1996) 267–289.
[2] V. Brailovski, F. Trochu, Bio-Med. Mater. Eng. 6 (1996) 291–298.
[3] K.R. Dai, Y.Y. Chu, Bio-Med. Mater. Eng. 6 (1996) 233–240.
[4] T.W. Duerig, A.R. Pelton, D. Stockel, Bio-Med. Mater. Eng. 6 (1996) 255–266.
[5] N.B. Morgan, Mater. Sci. Eng. A 378 (2004) 16–23.
[6] F. El Feninat, G. Laroche, M. Fiset, D. Mantovani, Adv. Eng. Mater. 4 (2002) 91–104.
[7] B. Thierry, M. Tabrizian, C. Trepanier, O. Savadogo, L.H. Yahia, J. Biomed. Mater. Res. 51 (4) (2000) 685–693.
[8] C.C. Shih, S.J. Lin, K.H. Chung, Y.L. Chen, Y.Y. Su, J. Biomed. Mater. Res. 52 (2) (2000) 323–332.
[9] C.C. Shih, S.J. Lin, Y.L. Chen, Y.Y. Su, S.T. Lai, G.J. Wu, C.F. Kwok, K.H. Chung, J. Biomed. Mater. Res. 52 (2) (2000) 395–403.
[10] O. Cisse, O. Savadogo, M. Wu, L. Yahia, J. Biomed. Mater. Res. 61 (3) (2002) 339–345.
[11] W.M. Carroll, M.J. Kelly, J. Biomed. Mater. Res. 67A (4) (2003) 1123–1130.
[12] S. Shabalovskaya, G. Rondelli, J. Anderegg, J.P. Xiong, M. Wu, J. Biomed. Mater. Res. B: Appl. Biomater. 69B (2) (2004) 223–231.
[13] J. Ryhanen, E. Niemi, W. Serlo, E. Niemela, P. Sandvik, H. Pernu, T. Salo, J. Biomed. Mater. Res. 35 (4) (1997) 451–457.
[14] M. Assad, L.H. Yahia, C.H. Rivard, N. Lemieux, J. Biomed. Mater. Res. 41 (1) (1998) 154–161.
[15] J. Ryhanen, M. Kallioinen, J. Tuukkanen, J. Junila, E. Niemela, P. Sandvik, W. Serlo, J. Biomed. Mater. Res. 41 (3) (1998) 481–488.
[16] C. Trepanier, T.K. Leung, M. Tabrizian, L. Yahia, J.G. Bienvenu, J.F. Tanguay, D.L. Piron, L. Bilodeau, J. Biomed. Mater. Res. 48 (2) (1999) 165–171.
[17] J.C. Wataha, P.E. Lockwood, M. Marek, M. Ghazi, J. Biomed. Mater. Res. 45 (3) (1999) 251–257.
[18] C.C. Shih, C.M. Shih, Y.L. Chen, Y.Y. Su, J.S. Shih, C.F. Kwok, S.J. Lin, J. Biomed. Mater. Res. 57 (2) (2001) 200–207.
[19] D.A. Armitage, T.L. Parker, D.M. Grant, J. Biomed. Mater. Res. 66A (1) (2003) 129–137.
[20] S.J. Simske, R. Sachdeva, J. Biomed. Mater. Res. 29 (4) (1995) 527–533.
[21] M. BergerGorbet, B. Broxup, C. Rivard, L.H. Yahia, J. Biomed. Mater. Res. 32 (2) (1996) 243–248.
[22] R.A. Ayers, S.J. Simske, T.A. Bateman, A. Petkus, R.L.C. Sachdeva, V.E. Gyunter, J. Biomed. Mater. Res. 45 (1) (1999) 42–47.
[23] M. Assad, P. Jarzem, M.A. Leroux, C. Coillard, A.V. Chernyshov, S. Charette, C.H. Rivard, J. Biomed. Mater. Res. B: Appl. Biomater. 64B (2) (2003) 107–120.
[24] M. Assad, A.V. Chernyshov, P. Jarzem, M.A. Leroux, C. Coillard, S. Charette, C.H. Rivard, J. Biomed. Mater. Res. B: Appl. Biomater. 64B (2) (2003) 121–129.
[25] J. Ryhanen, M. Kallioinen, W. Serlo, P. Peramaki, J. Junila, P. Sandvik, E. Niemela, J. Tuukkanen, J. Biomed. Mater. Res. 4447 (4) (1999) 472–480.
[26] W.Y. Jia, M.W. Beatty, R.A. Reinhardt, T.M. Petro, D.M. Cohen, C.R. Maze, E.A. Strom, M. Hoffman, J. Biomed. Mater. Res. 48 (4) (1999) 488–495.
[27] G. Riepe, C. Heintz, E. Kaiser, N. Chakfe, M. Morlock, M. Delling, H. Imig, Eur. J. Vasc. Endovasc. Surg. 24 (2) (2002) 117–122.
[28] T.S. Jacobs, J. Won, E.C. Gravereaux, P.L. Faries, N. Morrissey, V.J. Teodorescu, H.L. Hollier, M.L. Marin, J. Vasc. Surg. 37 (1) (2003) 16–26.
[29] D.E. Allie, C.J. Hebert, C.M. Walker, Endv. Today July/August (2004) 22–34.
[30] K.N. Melton, O. Mercier, Acta Metall. 27 (1979) 137–144.
[31] S. Miyazaki, T. Imai, Y. Igo, K. Otsuka, Metall. Trans. A 17 (1986) 115–120.
[32] D.Y. Li, X.F. Wu, T. Ko, Phil. Mag. A 63 (1991) 603–616.
[33] P.G. McCormick, Y. Liu, Acta Metall. Mater. 42 (1994) 2407–2413.
[34] L. Jordan, M. Masse, J.-Y. Collier, G. Bouquet, J. Alloys Compd. 211 (1994) 204–207.
[35] T.J. Lim, D.L. McDowell, J. Intell. Mater. Syst. Struct. 6 (1995) 817–830.
[36] B. Strnadel, S. Ohashi, H. Ohtsuka, T. Ishihara, S. Miyazaki, Mater. Sci. Eng. A 202 (1995) 148–156.
[37] Z. Xie, Y. Liu, J. Van, Humbeeck, Acta Mater. 46 (1998) 1989–2000.
[38] Z.H. Bo, D.C. Lagoudas, Int. J. Eng. Sci. 37 (1999) 1089–1140.
[39] D.C. Lagoudas, Z.H. Bo, Int. J. Eng. Sci. 37 (1999) 1141–1173.
[40] Z.H. Bo, D.C. Lagoudas, Int. J. Eng. Sci. 37 (1999) 1175–1203.
[41] Z.H. Bo, D.C. Lagoudas, Int. J. Eng. Sci. 37 (1999) 1205–1249.
[42] R.M. Tabanli, N.K. Simha, B.T. Berg, Mater. Sci. Eng. A 275 (1999) 644–648.
[43] T.J. Lim, D.L. McDowell, J. Eng. Mater. Technol. 121 (1999) 9–18.
[44] Y. Liu, I. Houver, H. Xiang, L. Bataillard, S. Miyazaki, Met. Mater. Trans. A 30 (1999) 1275–1282.
[45] K. Otsuka, C.M. Wayman, Shape Memory Materials, Cambridge University Press, 1998.
[46] R.H. Dauskardt, T.W. Duerig, R.O. Ritchie, in: K. Otsuka, K. Shimizu (Eds.), Shape Memory Materials, vol. 9, Materials Research Society, Pittsburgh, PA, 1989, pp. 243–249.
[47] A.L. McKelvey, R.O. Ritchie, J. Biomed. Mater. Res. 47 (3) (1999) 301–308.
[48] A.R. Pelton, X.Y. Gong, T.W. Duerig, SMST 2003, The International Conference on Shape Memory and Superelastic Technologies, Pacific Grove, CA, 2003, pp. 293–302.
[49] A.L. McKelvey, R.O. Ritchie, Metall. Mater. Trans. A: Phys. Metall. Mater. Sci. 32A (3) (2001) 731–743.
[50] P. Filip, K. Mazanec, Kovove Materialy-Met. Mater. 41 (5) (2003) 300–312.
[51] S.W. Robertson, R.O. Ritchie, Biomaterials 28 (4) (2007) 700–709.
[52] J. Stankiewicz, S. Robertson, R. Ritchie, J. Biomed. Mater. Res. 81A (3) (2007) 685–691.
[53] G. Eggeler, E. Hornbogen, A. Yawny, A. Heckmann, M. Wagner, Mater. Sci. Eng. A 378 (1–2) (2004) 24–33.
[54] M. Wagner, T.S. Sawaguchi, G. Kaustrater, D. Hoffken, G. Eggeler, Mater. Sci. Eng. A 378 (1–2) (2004) 105–109.
[55] G. Pompa, G. Gambarini, G. Pongione, G. Floridi, F. Di Carlo, M. De Luca, M. Quaranta, J. Dental Res. 79 (2000) 440–1440.
[56] G. Kuhn, L. Jordan, J. Endodont. 28 (10) (2002) 716–720.
[57] M. Wagner, J. Richter, J. Frenzel, D. Gronemeyer, G. Eggeler, Mater. Wiss. Werk. 35 (5) (2004) 320–325.
[58] J.M. Young, K.J. Van Vliet, J. Biomed. Mater. Res. 72B (1) (2005) 17–26.
[59] R.M. Tabanli, N.K. Simha, B.T. Berg, Metall. Mater. Trans. 32 (7) (2001) 1866–1869.
[60] M.A. Iadicola, J.A. Shaw, J. Intell. Mater. Syst. Struct. 13 (2002) 143–155.
[61] E. Hornbogen, J. Mater. Sci. 39 (2) (2004) 385–399.
[62] E. Hornbogen, A. Heckmann, Mater. Wiss. Werk. 34 (5) (2003) 464–468.

[63] A. Heckmann, E. Hornbogen, Mater. Sci. Forum 393–394 (2001) 325–328.
[64] V. Brailovski, P. Terriault, S. Prokoshkin, J. Mater. Eng. Perform. 11 (6) (2002) 614–621.
[65] C.P. Frick, A.M. Ortega, J. Tyber, K. Gall, H.J. Maier, Met. Mater. Trans. 35A (2004) 2013–2025.
[66] K. Gall, H. Sehitoglu, Y.I. Chumlyakov, I. Kireeva, Scripta Mater. 40 (1) (1999) 7–12.
[67] H. Sehitoglu, R. Anderson, I. Karaman, K. Gall, Y. Chumlyakov, Mater. Sci. Eng. A 314 (1–2) (2001) 67–74.
[68] K. Gall, H.J. Maier, Acta Mater. 50 (18) (2002) 4643–4657.
[69] J. Hurley, A.M. Ortega, J. Lechnaik, K. Gall, H.J. Maier, Z. Metall. 94 (2003) 547–552.
[70] R.L. Holtz, K. Sadananda, M.A. Imam, Int. J. Fatigue 21 (1999) S137–S145.
[71] American Society of Testing Materials, E8: Standard Test Methods for Tension Testing of Metallic Materials, in: ASTM Book of Standards, 2004.
[72] American Society of Testing Materials. I. Subcommittee E08.06, E647: Standard test method for measurement of fatigue crack growth rates, in: ASTM Book of Standards, 2005.
[73] C.P. Frick, K. Gall, A.M. Ortega, J. Tyber, H.J. Maier, A.El.M. Maksoud, Y. Liu, Mater. Sci. Eng. A 405 (2005) 34–49.
[74] P.K. Liaw, T.R. Leax, W.A. Logsdon, Acta Metall. 31 (10) (1983) 1581–1587.
[75] D. Taylor, A Compendium of Fatigue Thresholds and Growth Rates, Engineering Materials Advisory Services Ltd., London, 1985, p. 380.
[76] J. Van Humbeeck, J. Alloys Compd., Proceedings of the International Symposium on High Damping Materials, 2003, 355(1–2), pp. 58–64.
[77] M. Dolce, D. Cardone, Int. J. Mech. Sci. 43 (11) (2001) 2631–2656.
[78] Y. Liu, Z. Xie, J. Van Humbeeck, Mater. Sci. Eng. A 273–275 (1999) 673–678.
[79] R.O. Ritchie, Int. J. Fract. 100 (1) (1999) 55–83.
[80] C.F. Shih, J. Mech. Phys. Solids 29 (4) (1981) 305–326.
[81] L. Zhu, J.M. Fino, A.R. Pelton, Proceedings of the International Conference on Shape Memory and Superelastic Technologies, SMST, Pacific Grove, CA, USA, 2003.
[82] R.O. Ritchie, R.H. Dauskardt, W. Yu, A.M. Brendzel, J. Biomed. Mater. Res. 24 (2) (1990) 189–206.
[83] R.O. Ritchie, P. Lubock, J. Biomech. Eng., Trans. ASME 108 (1986) 153–160.